J. Fluid Mech. (2005), *vol.* 533, *pp.* 237–257.
doi:10.1017/S002211200500412X Printed in the United Kingdom

Stability of initially slow viscous jets driven by gravity

By ULRICH S. SAUTER AND HANS W. BUGGISCH

Institut für Mechanische Verfahrenstechnik und Mechanik, Universität Karlsruhe (TH), Germany

(Received 10 February 2004 and in revised form 24 January 2005)

The stability of vertically falling viscous liquid jets issuing from a circular orifice with a low fluid velocity where the flow is dominated by viscous effects torn down by gravity leading to a flow dominated by inertia far downstream, is studied by means of linear stability analysis as well as direct numerical simulation of the one-dimensional model. Jet stability is also studied experimentally. Results for marginal stability and critical frequencies are in excellent agreement with our theoretical predictions. A new global instability of a viscous jet is found. This instability is observable whenever a falling liquid jet exhibits a long enough viscosity dominated region. The source of instability is surface tension. In contrast to the Rayleigh capillary instability that is always present, but leads to very long disintegration lengths in highly viscous fluid jets, the instability described here only occurs when the volume flux falls below a certain limit depending on the fluid properties and the nozzle diameter.

1. Introduction

The stability of slender fluid jets has been studied quite extensively. First experimental studies on the decay of fluid jets were done by Savart (1833) who found small undulations growing on a jet of water by observing the jet with a simple stroboscopic method. He moved a black belt, interrupted by narrow white stripes, parallel to the jet. Plateau (1849) found that surface tension is responsible for jet decay. Confining himself mostly to the study of equilibrium shapes, he showed that long-wavelength perturbations reduce surface area and are thus favoured by surface tension. By means of linear stability analysis, Rayleigh (1878) found growth of sinusoidal perturbations on an infinitely long cylindrical jet was due to the competitive effects of surface tension and inertia that set the time scale $t_b^* = \sqrt{d^{*3}\,\rho/\gamma}$ of the breakup process. He found a wavelength of maximum growth rate, $\lambda_{crit}^* \approx 4.5\,d^*$ (where d^* is the diameter of the cylinder and dimensional variables are denoted by *) that determines the typical size of drops. Rayleigh (1892) also considered fluid viscosity. His work was extended by Weber (1931) and Chandrasekhar (1961) to take into account the whole Navier–Stokes equations, but still on cylindrical infinite jets and by means of linear stability analysis. Comparing his theoretical growth rates to experiments on disintegration lengths from Haenlein (1931), Weber gives an initial perturbation of $\ln(r_0^*/\delta^*) = 12$, where r_0^* is the initial jet radius and δ^* the initial amplitude of the perturbation. This correlation was refined by Grant & Middleman (1966) and Kitamura *et al.* (1987). Recent research on the decay of liquid jets still concentrates on the decay of initially cylindrical jets with a constant velocity primary solution. At a critical Weber number of $We = \gamma/(\rho\, r_0^*\, u_0^{*2}) \approx 0.32$ the inviscid jet becomes locally absolutely unstable at the orifice (Leib & Goldstein 1986*a*). Leib & Goldstein (1986*b*) also considered the local absolute transition in a viscous liquid jet without gravity. Following the conjecture

of Monkewitz (1990) that the transition to dripping of a fluid jet could be related to global instability, Le Dizès (1997) performs a global linear stability analysis of a falling capillary jet for Reynolds number $Re = r_0^* u_0^*/\nu \gg 1$ and Froude number $Fr = u_0^*/\sqrt{g r_0^*} \gg 1$. In an experimental study, Nonnenmacher (2003) empirically extends Weber's theory to take into account the gravitational effect in inertia dominated viscous jets.

The opposite limit of the stable jet in the presence of gravity is the dripping tap. Work on this problem started with Tate (1864) who measured drop weight and found a proportionality to the nozzle radius. Wilson (1988) gives a one-dimensional theory for the slow dripping of a viscous fluid, i.e. without considering inertia. For the transition from dripping to jetting of a jet with inertia and gravity, Clanet & Lasheras (1999) find a critical Weber number $We_c = \rho V_0^{*2} D^{*2}/\gamma$ as a function of the Bond number $Bo = \sqrt{\rho g D^{*2}/(2\gamma)}$ with one parameter depending on the fluid properties valid for $(\nu^2/g)^{1/3}/\sqrt{2\gamma/(\rho g)} < Bo < \pi/\sqrt{2}$. A historical overview on jet breakup and drop formation can be found in the extensive review by Eggers (1997). He comprehensively discusses the final nonlinear stages of drop separation.

Dynamics of jets with a strongly varying primary solution were first mentioned in studies on fibre spinning. Kase, Matsuo & Yoshimoto (1966) and Pearson & Matovich (1969) found independently that a Newtonian fibre becomes unstable to time-periodic disturbances when a critical drawdown ratio is exceeded. This phenomenon is called 'draw resonance'. The drawdown ratio is the ratio of take-up speed to nozzle speed. These studies only consider fluid viscosity. Pearson & Shah (1972) extended this theory to take into account inertia, surface tension and gravity that usually play a minor role in fibre spinning. They found that inertia and gravity aid stability while surface tension hinders stability. The growth of localized indentations in cross-sectional area that are convected down the fibre is known as 'necking' (Petrie & Denn 1976). The neck experiences a greater elongational tension than its surroundings and can be drawn down to zero cross-sectional area within fluid residence time in the fibre, provided the initial amplitude of the neck is large enough. More information on necking and fibre spinning can be found in Larson (1992).

The stability of very viscous jets of great but finite length drawn down by gravity remains unmentioned in literature on jet dynamics. Exiting slowly from a circular nozzle, these jets are dominated by viscous forces upstream and by inertial forces downstream. We want to study the stability behaviour of such jets in the presence of surface tension by means of linear stability analysis (§ 3) and stability experiments (§ 5.4).

The paper begins with a short derivation of the one-dimensional model and a brief discussion of the stationary solution (§ 2). Then the linear stability analysis is presented, followed by some nonlinear simulations of the basic equations in § 4. In §§ 5.1 and 5.2, the experimental set-up and the test fluids are presented. In § 5.3, the stationary contour is given for one representative experiment. The experimental stability results are given in § 5.4 followed by the development of a slenderness criterion restricting the validity of our theoretical predictions in § 5.6 and a comparison to related problems in § 6.

2. Basic equations

2.1. *The one-dimensional model*

The basic one-dimensional equations for the flow of a Newtonian fluid in a slender jet can be derived in many ways. Bechtel, Forest & Bogy (1986) and Bechtel, Lin & Forest

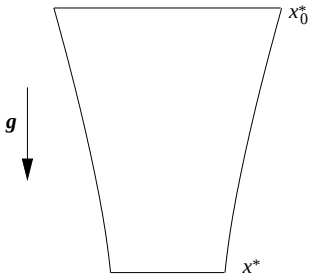

FIGURE 1. Section of a rotationally symmetric fluid jet.

(1987) developed slender jet asymptotics to any desired order, where the leading-order terms are the one-dimensional equations to be derived. Starting from the Navier–Stokes equations, Eggers (1997) uses a lubrication approximation to derive the one-dimensional equations. We want to derive these equations starting from integral balances. In contrast to the lubrication theory this makes it easy to derive equations for non-Newtonian fluids as no *a priori* assumptions have to be made concerning the constitutive equation.

Figure 1 shows the section of the jet to be balanced. The following assumptions are made in the one-dimensional theory:

(i) The jet is axisymmetric.
(ii) The jet is slender with slowly varying cross-sectional area.
(iii) The only relevant velocity component points in the axial direction.
(iv) The flow is purely extensional.
(v) The fluid is incompressible.

For this type of flow, the mass balance for the jet section shown in figure 1 is

$$\int_{x_0^*}^{x^*} \frac{\partial a^*}{\partial t^*} \mathrm{d}x^* = a_0^* u_0^* - a^* u^*. \tag{2.1}$$

The dimensional variables are denoted by *. a^*, u^* and x^* are dimensional cross-sectional area, axial velocity and axial coordinate, respectively. Zero subscripts denote values at the nozzle exit. Differentiation of (2.1) to x^* gives

$$\frac{\partial a^*}{\partial t^*} + \frac{\partial (a^* u^*)}{\partial x^*} = 0. \tag{2.2}$$

The momentum balance is

$$\frac{\mathrm{D}}{\mathrm{D}t^*} \int_{x_0^*}^{x^*} \rho a^* u^* \mathrm{d}x^* = F^* + g \int_{x_0^*}^{x^*} \rho a^* \mathrm{d}x^*. \tag{2.3}$$

For an uniaxial extensional flow, the Newtonian constitutive equation

$$\boldsymbol{T}_E^* = 2\eta \boldsymbol{D}^* \tag{2.4}$$

reduces to

$$\tau_{xx}^* - \tau_{rr}^* = \eta_D \frac{\partial u^*}{\partial x^*}, \tag{2.5}$$

where $\eta_D = 3\eta$ denotes the extensional viscosity. In a slender jet, the curvature in the axial direction is negligible against the radial curvature, therefore:

$$-\tau_{rr}^* = \frac{\gamma}{R^*}. \tag{2.6}$$

The force $F^*(x^*, t^*)$ acting at a position x^* and at a time t^* in the axial direction on the jet is given by

$$F^* = a^* \tau^*_{xx} + 2\pi R^* \gamma \tag{2.7}$$

where the last term on the right-hand side results from the 'membrane tension' in the jets 'shell'. Using the simple correlation between radius and cross-sectional area $R^* = \sqrt{a^*/\pi}$, we obtain

$$F^* = \eta_D a^* \frac{\partial u^*}{\partial x^*} + \gamma \sqrt{\pi} \sqrt{a^*}. \tag{2.8}$$

Incorporating this and the mass balance into (2.3), we obtain after differentiation to x^*,

$$\frac{\partial u^*}{\partial t^*} + u^* \frac{\partial u^*}{\partial x^*} = \frac{\eta_D}{\rho} \frac{\partial \left(a^* \dfrac{\partial u^*}{\partial x^*} \right)}{\partial x^*} \frac{1}{a^*} + \frac{\gamma \sqrt{\pi}}{\rho} \frac{\partial \sqrt{a^*}}{\partial x^*} \frac{1}{a^*} + g. \tag{2.9}$$

The following dimensionless variables are introduced:

$$t = \left(\frac{\rho g^2}{\eta_D} \right)^{1/3} t^*, \quad x = \left(\frac{\rho^2 g}{\eta_D^2} \right)^{1/3} x^*, \quad u = \left(\frac{\rho}{\eta_D g} \right)^{1/3} u^*, \quad a = \left(\frac{\eta_D^2 g^2 \rho}{\pi^{3/2} \gamma^3} \right)^{2/3} a^*. \tag{2.10}$$

Using these new variables, the mass and momentum balances can be written in a very compact form:

$$a_t + (au)_x = 0, \tag{2.11}$$

$$u_t + u u_x = \frac{(a u_x)_x}{a} + \frac{\sqrt{a}_x}{a} + 1. \tag{2.12}$$

2.2. *Stationary solution*

For the stationary solution we want to restrict our citations to studies that include at least viscosity, inertia and gravity. There are many excellent studies on inviscid jets but summarising them would go beyond the scope of this study.

Clarke (1966) gives an analytical stationary solution for a semi-infinite Newtonian jet without surface tension tending to the free-fall velocity $u^* = \sqrt{2gx^*}$ far downstream. This downstream boundary condition for semi-infinite jets was confirmed by Kaye & Vale (1969) for Newtonian and by Joseph, Nguyen & Matta (1983) for non-Newtonian fluids. The presence of surface tension slightly changes this stationary solution, that is considered by Clarke (1969) with an approximate correction.

Since our stability analysis is carried out numerically, there is no need for an approximate stationary solution and we decided to integrate the stationary equations numerically. In the following, we want to give some insight into the stationary solution field not presented elsewhere.

In the stationary case, (2.11) and (2.12) become

$$(\tilde{a}\tilde{u})_x = 0 \tag{2.13}$$

and

$$\tilde{u}\tilde{u}_x = \tilde{u}_{xx} + \frac{\tilde{a}_x \tilde{u}_x}{\tilde{a}} + \frac{1}{2} \frac{\tilde{a}_x}{\tilde{a}^{3/2}} + 1, \tag{2.14}$$

where stationary quantities are denoted by a tilde. Equation (2.13) can be integrated right away, which leads to

$$\tilde{a}\tilde{u} = q = \text{const.} \tag{2.15}$$

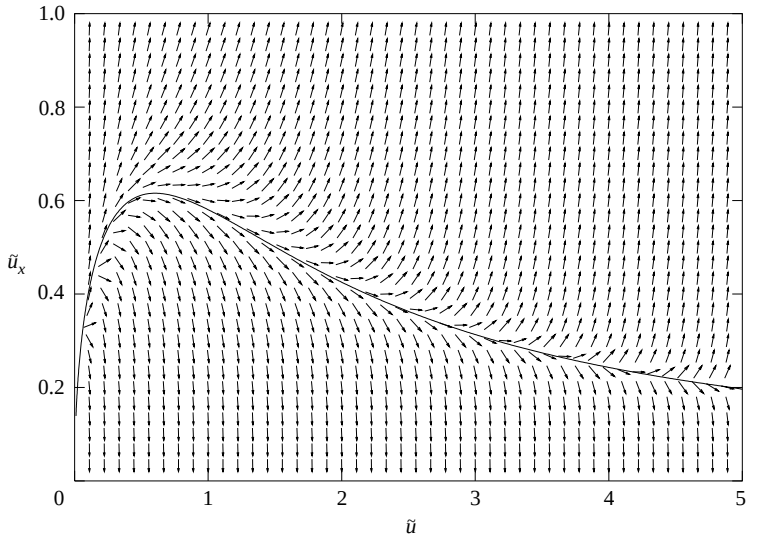

FIGURE 2. Solution field and stationary solution for $q = 1000$.

Incorporating this and (2.13) into (2.14) we obtain

$$\tilde{u}\tilde{u}_x = \tilde{u}_{xx} - \frac{\tilde{u}_x^2}{\tilde{u}} - \frac{1}{2}\frac{\tilde{u}_x}{\sqrt{q}\sqrt{\tilde{u}}} + 1. \tag{2.16}$$

The solution field of this equation, which can of course be rewritten as a system of two ordinary differential equations of first order, can be seen in figure 2. The solution field diverges as $\tilde{u}$ and x increase, therefore (2.16) has to be integrated backwards, which means from the downstream boundary upwards. The stationary solution shows a viscosity dominated domain for small $\tilde{u}$, where $\tilde{u} \sim x^2$ and an inertia dominated domain for large $\tilde{u}$, where $\tilde{u}$ approaches $\sqrt{2x}$, the free-fall velocity. In figure 2, this behaviour can be seen through $\tilde{u}_x \sim \sqrt{\tilde{u}}$ for small $\tilde{u}$ and $\tilde{u}_x \sim 1/\tilde{u}$ for large $\tilde{u}$. These are the asymptotes of Clarke's analytical stationary solution without surface tension (Clarke 1966). The transition from viscosity to inertia dominated flow occurs for $\tilde{u}$ and x of order unity. The characteristic length for the location of the transition can be extracted from (2.10), it is $(\eta_D^2/\rho^2 g)^{1/3}$.

For long jets, the downstream boundary condition only affects the stationary solution within about one dimensionless length upstream. Figure 2 displays only the general stationary behaviour. $\tilde{u}_x = 0$ is chosen as the downstream boundary condition, but far to the right, outside the diagram. For smaller values of q that correspond to greater influence of surface tension, the maximum value of $\tilde{u}_x$ is lower, but there is still a viscosity dominated domain for small $\tilde{u}$ and an inertia dominated domain for large $\tilde{u}$.

3. Linearized stability analysis

3.1. *Direct numerical simulation*

Operating with linearized stability analysis on a stationary solution of a dynamical system, we obtain stability criteria for infinitesimal disturbances. Whether these criteria hold for finite disturbances or not cannot be predicted using a linearized theory. Experiments or nonlinear analyses have to be performed to answer this question.

Following standard procedures, a perturbation ansatz

$$a(x,t) = \tilde{a}(x)(1+\alpha(x,t)), \tag{3.1}$$

$$u(x,t) = \tilde{u}(x)(1+\beta(x,t)), \tag{3.2}$$

is made. Incorporating this ansatz into (2.11) and (2.12), we obtain after linearization in α and β

$$\beta_t = \beta_{xx} + \left(-\tilde{u} + \frac{\tilde{u}_x}{\tilde{u}}\right)\beta_x + \left(\frac{\tilde{u}_x}{2\tilde{u}\sqrt{q\tilde{u}}} - \tilde{u}_x - \frac{1}{\tilde{u}}\right)\beta + \left(\frac{1}{2\sqrt{q\tilde{u}}} + \frac{\tilde{u}_x}{\tilde{u}}\right)\alpha_x + \left(\frac{\tilde{u}_x}{4\sqrt{q}\,\tilde{u}^{3/2}}\right)\alpha, \tag{3.3}$$

$$\alpha_t = -\tilde{u}\beta_x - \tilde{u}\alpha_x. \tag{3.4}$$

These equations are solved using the following boundary conditions:

$$a(0,t) = a_0, \quad u(0,t) = u_0, \quad u_x(l,t) = 0. \tag{3.5}$$

Herein, $x = l$ denotes the lower end of the jet.

A finite jet has to end somewhere, impacting on a plate or on a free fluid surface. Let the jet impact on a plate. As it approaches the plate, the acceleration of the jet will change sign from + to −. Taking $u_x(l,t) = 0$ implies the assumption that the axial position at which this change of sign takes place is fixed. If the jet is very long, this assumption is justified since it has no effect on the stability properties, as we will see later by varying the theoretical jet length.

We have to point out, that the chosen downstream boundary condition $u_x(l,t) = 0$ is not realistic. In viscous liquid jets, buckling and coiling is observed under certain conditions (see for instance Mahadevan, Ryu & Samuel 1998, or Tchavdarov, Yarin & Radev 1993). In our experiments, we observe coiling at the lower end of the jet that does not change the stability behaviour of the whole jet. Varying our experimental jet length between 0.5 m and 2 m led to the same critical flow rates and corresponding critical frequencies.

Applied to the stationary variables, boundary conditions (3.5) read

$$\tilde{a}(0) = a_0, \quad \tilde{u}(0) = u_0, \quad \tilde{u}_x(l) = 0. \tag{3.6}$$

For the perturbation variables we obtain

$$\beta(0,t) = 0, \quad \beta_x(l,t) = 0. \tag{3.7}$$

We introduce an initial perturbation through

$$\alpha(0,t) = \begin{cases} \delta\left(1 - \cos^2\left(\pi\dfrac{t}{t_1}\right)\right), & 0 \leqslant t \leqslant t_1, \\ 0, & t > t_1, \end{cases} \tag{3.8}$$

where δ is an arbitrary initial amplitude (we are dealing with homogenous linear equations) and t_1 is a short time. t_1 is chosen 0.001 times the fluid residence time in the stationary jet $t_{res} = \int_0^l 1/\tilde{u}\,\mathrm{d}x$.
The initial conditions are:

$$\alpha(x,0) = 0, \quad \beta(x,0) = 0. \tag{3.9}$$

A numerical method using an implicit Euler scheme for the second derivative and an explicit upwind scheme for the conservative part is used to solve the equations. Points

of marginal stability are sought by applying a Newton's-method with relaxation on the growth rate of the perturbation variables. Exponential growth, or decay, respectively, is expected and observed. These calculations are extremely tedious, even on state-of-the-art computers, because fine discretization is necessary in order to produce accurate results.

3.2. *Separation ansatz*

Therefore another method is used to calculate more points of marginal stability. Chronologically this method was tried first, but without very good initial values it was impossible to find a solution.

We perform the following transformation that results in a strong stretching of the downstream coordinate for small x.

$$\tau = \tau_0 + \int_{x_0}^{x} \frac{\mathrm{d}x}{\tilde{u}}, \tag{3.10}$$

τ is a Lagrangian-coordinate in the stationary case. Operating on (2.16), we obtain

$$\tilde{u}_{\tau\tau} = \tilde{u}^2\tilde{u}_\tau + 2\frac{\tilde{u}_\tau^2}{\tilde{u}} - \frac{\sqrt{\tilde{u}}\tilde{u}_\tau}{2\sqrt{q}} - \tilde{u}^2. \tag{3.11}$$

Transformation (3.10) is applied to (3.3) and (3.4) and periodic solutions of exponential growth in time are sought. This is done by a separation ansatz:

$$\alpha(\tau, t) = \mathrm{e}^{\lambda t}(\alpha_1(\tau)\sin(\omega t) + \alpha_2(\tau)\cos(\omega t)), \tag{3.12}$$

$$\beta(\tau, t) = \mathrm{e}^{\lambda t}(\beta_1(\tau)\sin(\omega t) + \beta_2(\tau)\cos(\omega t)). \tag{3.13}$$

Introducing

$$\varphi_1(\tau) = \frac{\mathrm{d}\beta_1(\tau)}{\mathrm{d}\tau}, \tag{3.14}$$

$$\varphi_2(\tau) = \frac{\mathrm{d}\beta_2(\tau)}{\mathrm{d}\tau}, \tag{3.15}$$

we obtain a system of first-order ordinary differential equations for the amplitude functions $\alpha_1, \alpha_2, \beta_1, \beta_2, \varphi_1$ and φ_2:

$$\alpha_{1\tau} = -\varphi_1 - (\lambda\alpha_1 - \omega\alpha_2), \tag{3.16}$$

$$\alpha_{2\tau} = -\varphi_2 - (\lambda\alpha_2 + \omega\alpha_1), \tag{3.17}$$

$$\beta_{1\tau} = \varphi_1, \tag{3.18}$$

$$\beta_{2\tau} = \varphi_2, \tag{3.19}$$

$$\begin{aligned}\varphi_{1\tau} = {} & \left(\left(\frac{1}{2}\sqrt{\frac{\tilde{u}}{q}} + \frac{\tilde{u}_\tau}{\tilde{u}}\right)\lambda - \frac{\tilde{u}_\tau}{4\sqrt{q\tilde{u}}}\right)\alpha_1 - \left(\frac{1}{2}\sqrt{\frac{\tilde{u}}{q}} + \frac{\tilde{u}_\tau}{\tilde{u}}\right)\omega\alpha_2 \\ & + \left(\lambda\tilde{u}^2 + \tilde{u} + \tilde{u}\tilde{u}_\tau - \frac{\tilde{u}_\tau}{2\sqrt{q\tilde{u}}}\right)\beta_1 - \omega\tilde{u}^2\beta_2 + \left(\tilde{u}^2 + \frac{1}{2}\sqrt{\frac{\tilde{u}}{q}} + \frac{\tilde{u}_\tau}{\tilde{u}}\right)\varphi_1,\end{aligned} \tag{3.20}$$

$$\begin{aligned}\varphi_{2\tau} = {} & \left(\left(\frac{1}{2}\sqrt{\frac{\tilde{u}}{q}} + \frac{\tilde{u}_\tau}{\tilde{u}}\right)\lambda - \frac{\tilde{u}_\tau}{4\sqrt{q\tilde{u}}}\right)\alpha_2 + \left(\frac{1}{2}\sqrt{\frac{\tilde{u}}{q}} + \frac{\tilde{u}_\tau}{\tilde{u}}\right)\omega\alpha_1 \\ & + \left(\lambda\tilde{u}^2 + \tilde{u} + \tilde{u}\tilde{u}_\tau - \frac{\tilde{u}_\tau}{2\sqrt{q\tilde{u}}}\right)\beta_2 + \omega\tilde{u}^2\beta_1 + \left(\tilde{u}^2 + \frac{1}{2}\sqrt{\frac{\tilde{u}}{q}} + \frac{\tilde{u}_\tau}{\tilde{u}}\right)\varphi_2.\end{aligned} \tag{3.21}$$

Equation (3.11) is rewritten in terms of two first-order equations and the parameters q, ω, λ and falling distance x are introduced as differential equations.

$$\tilde{u}_\tau = \tilde{v}, \tag{3.22}$$

$$\tilde{v}_\tau = \tilde{u}^2\tilde{v} + 2\frac{\tilde{v}^2}{\tilde{u}} - \frac{\sqrt{\tilde{u}}\tilde{v}}{2\sqrt{q}} - \tilde{u}^2, \tag{3.23}$$

$$x_\tau = \tilde{u}, \tag{3.24}$$

$$q_\tau = 0, \tag{3.25}$$

$$\omega_\tau = 0, \tag{3.26}$$

$$\lambda_\tau = 0. \tag{3.27}$$

Together with (3.17) to (3.21), we obtain a system of 12 ordinary differential equations to be solved simultaneously. Points of marginal stability are obtained for $\lambda = 0$. The boundary conditions are

$$\left.\begin{array}{rr} \tilde{u}(\tau=0)=u_0, & \tilde{v}(\tau=T)=0, \\ x(\tau=0)=0, & \alpha_1(\tau=0)=0, \\ \alpha_2(\tau=0)=0, & \beta_1(\tau=0)=0, \\ \beta_2(\tau=0)=0, & \varphi_1(\tau=T)=0, \\ \varphi_2(\tau=T)=0, & \lambda(\tau=T)=0, \end{array}\right\} \tag{3.28}$$

where $\tau = T$ denotes the lower end of the jet. The differential equations (3.17) to (3.21) are homogeneous, first-order and linear in $\alpha_1, \alpha_2, \beta_1, \beta_2, \varphi_1$ and φ_2, therefore arbitrary multiples of these functions are solutions to (3.17) to (3.21). This implies that one of the function values and one phase at a position τ can be chosen arbitrarily, e.g.

$$\alpha_1(\tau = T) = 1, \tag{3.29}$$

$$\alpha_2(\tau = T) = 0. \tag{3.30}$$

The equations are solved using a multiple shooting scheme according to Stoer & Bulirsch (1978) using a Runge–Kutta–Fehlberg method as integrator. Initial data is taken from the numerical simulation of the partial differential equations described above.

For long jets there is only one free parameter on the line of marginal stability: either u_0 or q or ω can be fixed, the remaining parameters are obtained from the solution of the differential equations. After one point of marginal stability is found, others are sought by taking the current solution as initial values and slightly varying one of the parameters (e.g. u_0). Following this procedure, we obtain a stability, diagram as shown in figure 3. For each calculated point on the line of marginal stability, the dimensionless jet length is doubled until the relative change in the critical parameters falls below a given limit (typically 10^{-3}). This was already often reached when doubling the dimensionless length from 10 to 20.

The fit function,

$$a_{0,crit}(u_0) = 0.025u_0^{-2.51}, \tag{3.31}$$

given in figure 3 approximates the calculated line of marginal stability reasonably well and should be useful for engineering purposes.

We have found a line of marginal stability for the temporal instability of a long but finite liquid jet with viscosity, inertia, surface tension and gravity. The jet shows time-periodic diameter oscillations when for a given nozzle radius and given fluid

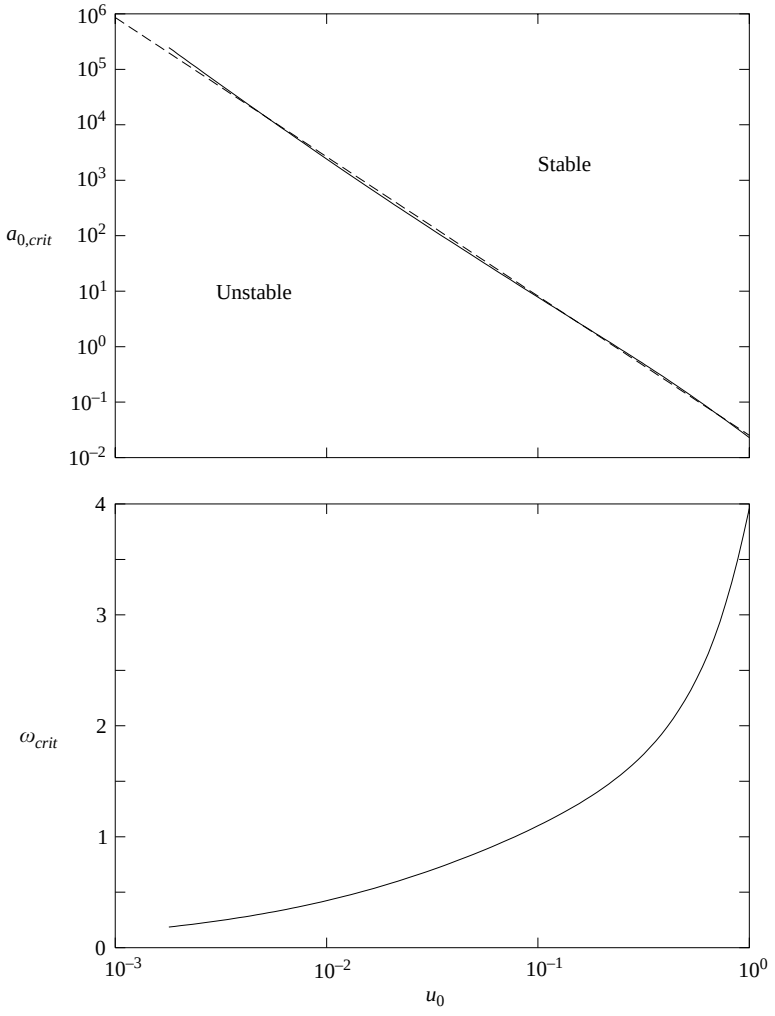

FIGURE 3. Line of marginal stability and corresponding critical angular frequency for a Newtonian fluid. —, linearized stability analysis; - - -, approximative fit.

properties, e.g. given a_0, the outflow velocity, or volume flux, respectively, falls below a certain limit. The oscillation shows a well-defined angular frequency.

The amplitude $\sqrt{\alpha_1^2 + \alpha_2^2}$ of the marginally stable oscillation rises with growing fluid residence time. The growth is less pronounced for large values of q that correspond to low influence of surface tension. This growing amplitude can lead to jet breakup somewhere far downstream that can be interpreted as a connection to the Rayleigh capillary instability. In our analysis the initial amplitude is zero, therefore the calculation of breakup lengths from an initial disturbance is not possible with our ansatz and is not the aim of this paper. Our finite jet length prevents the infinite growth of instabilities that grow with fluid residence time. The case of vanishing viscosity cannot be captured by our analysis because fluid viscosity is used for our non-dimensionalization. Moreover, for any finite non-dimensional jet length, the dimensional jet length tends to zero for vanishing viscosity.

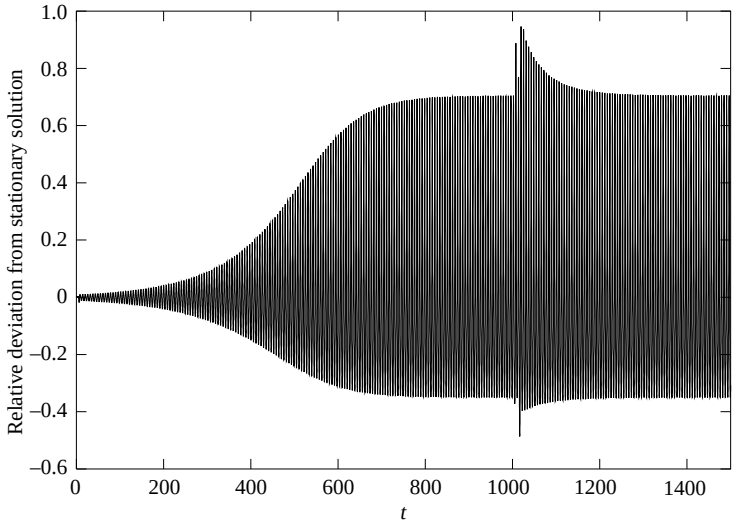

FIGURE 4. $(a(2.5,t)-\tilde{a}(2.5))/(\tilde{a}(2.5))$ for an unstable set of parameters: $u_0=0.1$, $l=10.0$, $q=0.7$. At $t=1000$, a disturbance is introduced at the outflow.

4. Simulation of the nonlinear equations

There exist many nonlinear studies on liquid jets (Eggers 1997), but they are mostly concerned with the breakup of jets. We are not aware of nonlinear studies on long viscous gravity-driven jets.

In order to check whether our results obtained by linear stability analysis hold in the nonlinear regime (2.11) and (2.12) are integrated numerically. For this purpose, a combined implicit/explicit finite-difference scheme is used. The first-order derivatives are integrated using an explicit upwind method and the viscous terms are integrated via an implicit Euler scheme.

The jet length is chosen as $l=10$, because at greater length there is no change in stability behaviour for the upper part of the jet. Oscillation frequencies and amplitudes remain the same at $x<5$ for jets of length 20 and 50. A length of 10 is sufficiently long for no backlash of the downstream boundary to affect the jet behaviour upstream. The amplitude of the oscillation rises with axial position possibly leading to jet breakup somewhere downstream. This is not analysed systematically.

Figure 4 shows the relative deviation of the jet cross-section from the stationary solution as a function of time for an unstable set of parameters. The initial amplitude results from the accuracy difference of the stationary solution calculated with a Runge–Kutta–Fehlberg solver and the transient solver. This accuracy difference acts as a small δ-pulse at every vertical position in the jet. The amplitude reaches an upper limit at large time values for initial amplitudes below or above this limit. This is called a limit cycle. At $t=1000$, a disturbance is introduced by increasing the initial jet cross-sectional area by 1 % for $\Delta t=10$. The oscillation amplitude exceeds the limit cycle value for a short time and returns to the limit cycle. Fourteen stages of one period in the limit cycle can be seen in figure 5 for the whole jet. The vertical axis is contracted strongly (by a factor of several hundred for a highly viscous fluid). Thick regions are shorter than thin regions. In figure 6, the relative deviation from the stationary solution in a and u is given for the whole jet at seven stages of one period in the limit cycle (every other in figure 5). The amplitude of the oscillation

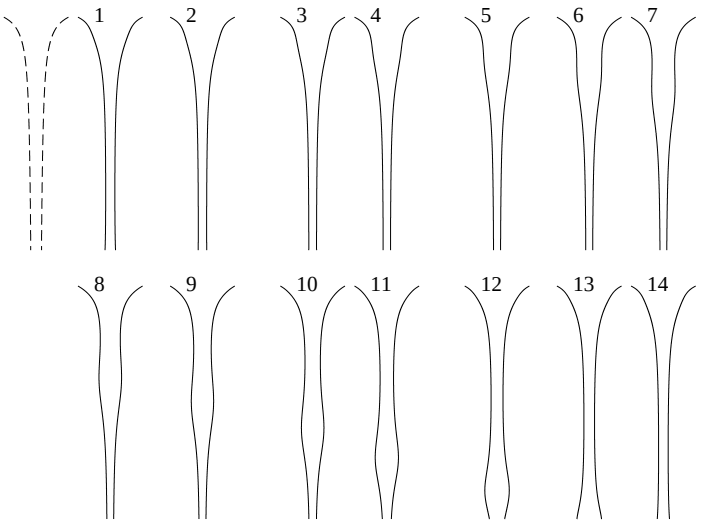

FIGURE 5. Stages of one period in the limit cycle of figure 4. - - -, stationary solution.

in the cross-sectional area rises with axial position possibly leading to breakup for longer jets. The wavelength also rises with axial position as the jet becomes more and more stretched. The amplitude of the oscillation of the relative deviation from the stationary solution in axial velocity rises initially and then almost stagnates. The amplitude of the absolute deviation from the stationary solution in axial velocity still rises, however, since the axial velocity rises.

For a stable set of parameters slightly above the line of marginal stability (e.g. $u_0 = 0.1$, $l = 10.0$, $q = 0.77$) the initial amplitude is about the same as for the unstable set of parameters shown in figure 4, but decays rapidly. Similar simulations were carried out slightly above and slightly below the line of marginal stability for several randomly selected u_0 in the range of $0.01 < u_0 < 0.1$. No subcritical bifurcating solutions being unstable in the linearly stable regime could be found. In the linearly unstable regime, limit cycles are found in the neighbourhood of the line of marginal stability, suggesting a Hopf-type supercritical bifurcation. Further in the linearly unstable regime, the cross-sectional area reaches zero at some point and numerics breaks down. Simulations for $u_0 < 0.01$ are tedious, because of the time-step limiting CFL-condition and the required fine axial discretization and therefore were not carried out.

Further in the stable regime, no time periodic oscillations are observed. When a square pulse in the cross-sectional area is introduced at the nozzle, a compact wave package travels through the jet with rising amplitude. This is a convective instability that corresponds to a temporal growth in the comoving frame of reference. It seems to be connected to the Rayleigh capillary instability. The wavelength of this perturbation is much shorter than the wavelengths occurring in our instability. If the jet is very long (e.g. $l \gg 100$) or the initial amplitude is very large, jet breakup occurs in our simulations, and numerics breaks down. To obtain meaningful disintegration lengths from the simulations, it would be necessary to include the axial curvature into the surface-tension term of the one-dimensional theory that becomes relevant at large amplitudes and short wavelengths. This is not considered in our study.

The Rayleigh capillary instability is present in any liquid jet. High viscosity and gravity reduce its growth rate, which leads to very large disintegration lengths of 100 m or more in highly viscous jets subject to ubiquitous small fluctuations

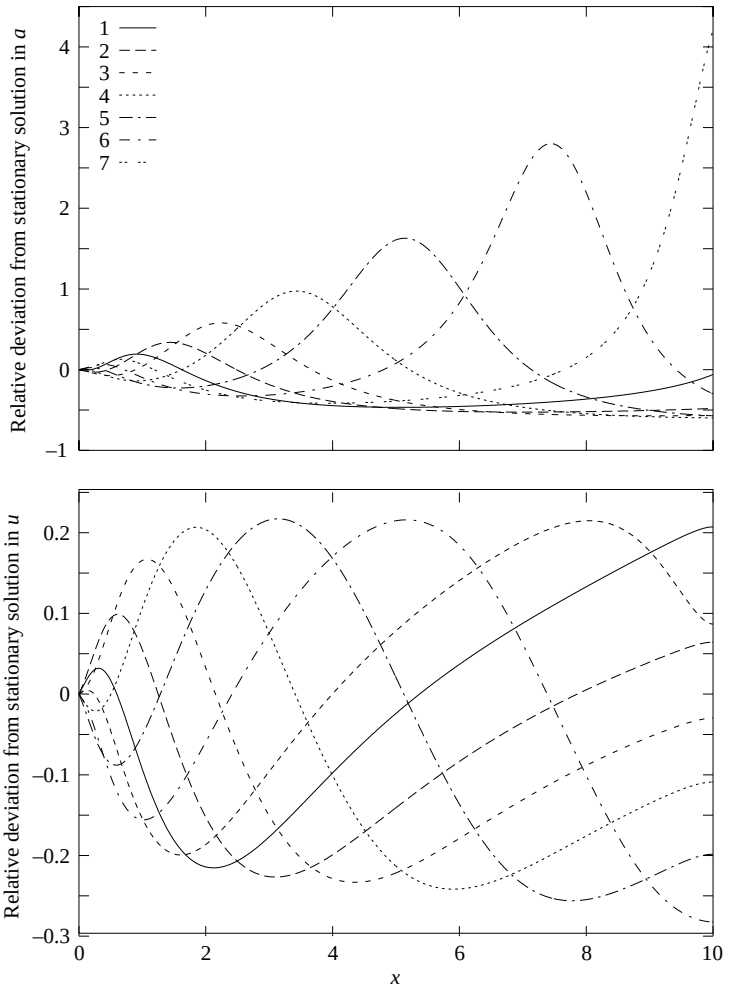

FIGURE 6. Relative deviation from the stationary solution $(a(x,t)-\tilde{a}(x))/(\tilde{a}(x))$ and $(u(x,t)-\tilde{u}(x))/(\tilde{u}(x))$ at seven equally spaced times of one period in the limit cycle of figure 4: $u_0=0.1$, $l=10.0$, $q=0.7$.

(Nonnenmacher 2003). Therefore, the Rayleigh capillary instability will only be observed in highly viscous jets, if the jet is subject to forced oscillations.

In our experiments, we observed jet breakup within our falling distance of 2 m for the fluid of lowest viscosity (AK1000) at low flow rates in our linearly stable and unstable regimes. By repeating the experiments at a jet length of 0.5 m, where no jet breakup occurred, we found that this breakup at the lower end of the jet does not affect our instability. The Rayleigh capillary instability and the global instability we found seem to occur independently of each other.

5. Experiments

5.1. *Experimental set-up*

The experimental apparatus (figure 7) consists of two independent units, the fluid cycle and the optical system. In the fluid cycle, the test fluid is stored in a reservoir.

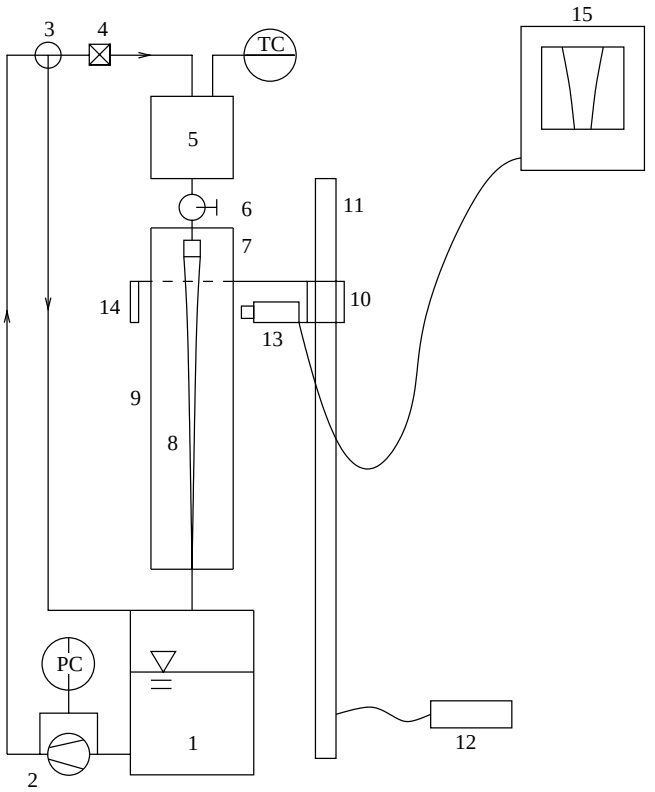

FIGURE 7. Sketch of the experimental setup. 1, reservoir; 2, gear pump; 3, pressure relief valve with bypass; 4, filter; 5, equalizing tank; 6, valve; 7, exchangeable nozzle; 8, fluid jet; 9, evacuated glass tube; 10, slide with x, y-table; 11, linear guides; 12, absolute length encoder; 13, CCD-camera; 14, back lighting; 15, computer with frame grabber. TC, temperature control; PC, pressure control.

This reservoir feeds an adjustable gear pump suited for low flow rates as it is usually used in laboratory scale spinline experiments. Gear pumps of this type have a low pulsation that is damped away in the flexible tube and the equalizing tank upstream of the nozzle. For safety reasons, a series connection of a pressure relief valve with bypass and a filter is set between the flexible tube and the equalizing tank. Impurities of, for example, sealing compound could close the nozzle, leading to the maximum pressure of the pump in the apparatus that is about 300 bars. That would damage the pressure and temperature transducers and possibly the whole apparatus. The nozzle exit leads the fluid jet into an evacuated vertical glass tube with a height of 2 m, where the jet is stretched by gravitational forces with negligible influence of air friction and air movement. The shear stress acting on the jet owing to air friction can be estimated using an empirical correlation set up in the context of fibre spinning by Kase & Matsuo (1967). Comparison with other active forces, namely the gravitational force, gives the necessary level of evacuation. During the experiments, we found out that the level of evacuation has only a little influence on the experimental results, the lower faster end of the jet where air friction is relevant having virtually no reaction to the upper slower part of the jet defining the stability properties. A hole in the bottom of the glass tube lets the jet fall into the reservoir. The brass nozzles have

Test fluid	η (Pa s)	ρ (kg m^{-3})	γ (N m^{-1})
AK1000	1.39	976	0.020
AK5000	5.32	963	0.020
AK10000	10.7	963	0.020
AK50000	58.5	963	0.021

TABLE 1. Shear viscosity, density and surface tension of the test fluids at 21°C.

a long conical contraction zone leading smoothly into a cylindrical tube that is five nozzle exit diameters long with a sharp edge at the exit. The sharp edge has an outer cone with an opening angle of 30° to 45° to the vertical axis. If the opening is flat, the test fluid creeps horizontally outward from the nozzle exit, leading to a greater and undefined effective nozzle diameter. The sharp edge prevents this phenomenon showing the desired well-defined outflow conditions. Nozzles of the diameters 0.51, 1.02, 1.51, 1.55, 2.10, 2.55, 3.12 and 4.06 mm are used for the experiments. The smallest three nozzle openings are manufactured by spark erosion, the others are drilled.

The optical system consists of a CCD-camera with strongly magnifying macro zoom optics (at maximum magnification 0.82 μm per pixel) and backlighting mounted together on an x, y-table. The x, y-table is mounted on a slide and is vertically adjustable on linear guides. An absolute length encoder gives the current vertical position. The digital images are captured by a frame grabber and analysed on a computer. From the grey-scale digital images, the jet diameter information can be extracted by use of a steepest grey-scale gradient method. The jet diameter can be determined within an uncertainty of about one pixel at a total diameter of several hundred pixels.

5.2. *Test fluids*

The test fluid is linear silicone oil of different viscosity levels, exhibiting constant shear viscosity in a rotational rheometer for shear rates between 0.1 s^{-1} and 100 s^{-1}. Rheometer data can be found in table 1. The maximum dimensionless extensional rate in a gravity-driven jet is approximately 0.62, giving actual maximum strain rates of 8 s^{-1} (AK50000) to 17 s^{-1} (AK1000). For low enough shear and extensional rates, these silicone oils can be considered as Newtonian fluids. Fluid density was determined using a method based on Archimedes' principle. Surface tension was measured using the Wilhelmy Plate method.

All experiments are carried out in a temperature range of 20 °C–22 °C. The fluid temperature in the equalizing tank is recorded. The glass transition temperature T_g and the coefficient of thermal expansion α_l of a polymeric liquid show approximately an empirical correlation $\alpha_l T_g \approx 0.16$ (Boyer & Spencer 1944). The glass transition temperature of silicone oil is approximately 150 K (van Krevelen 1990). Therefore, silicone oil density decreases 0.1 % per K, which is negligible under the experimental conditions. Guggenheim (1945) found a relationship for the temperature dependence of the interfacial tension $\gamma(T) = \gamma_0(1 - T/T_k)^{(11/9)}$. Together with data from Wu (1982) for $\gamma_0 = 0.0353$ N m^{-1} and $T_k = 776$ K, we can estimate the relative change in γ per K, which turns out to be about -0.25 % K^{-1} at 21 °C. This is greater than the density change, but still negligible. Van Krevelen (1990) gives $\log(\eta(T)/\eta(1.2T_g)) = A(T/T_g - 1)$ with $T_g = 150$ K and $A = 5.2$ for silicone oil. The relative change in viscosity per K is therefore -2.1 % K^{-1} at 21 °C. This is not negligible and has to be compensated.

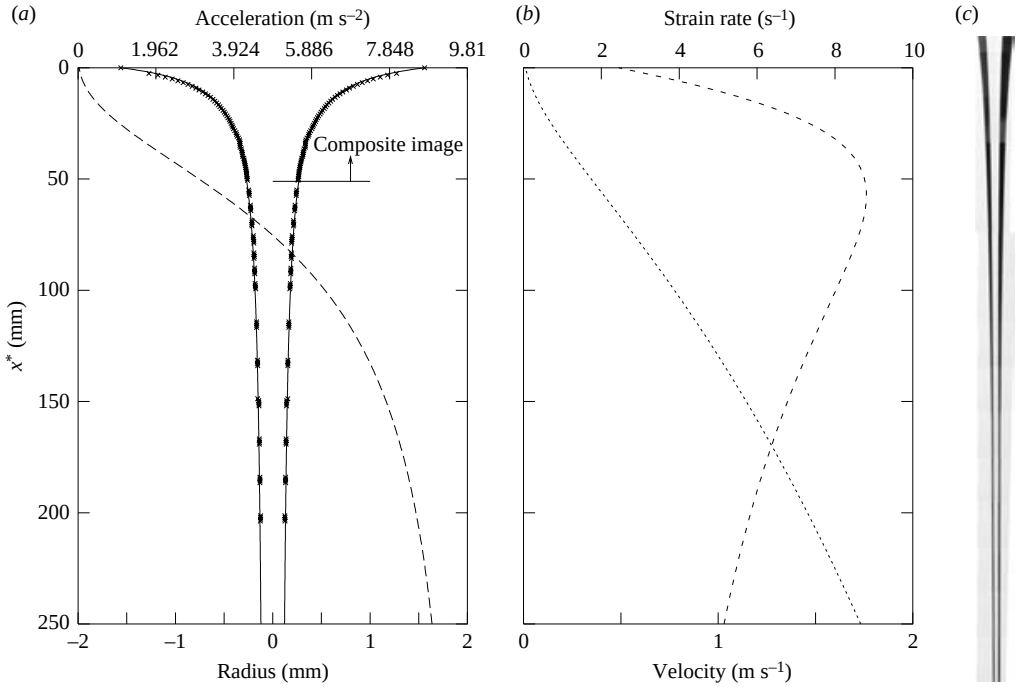

FIGURE 8. Stationary jet. AK10000, $d^* = 3.12\,\text{mm}$, $\dot{V}^* = 8.06 \times 10^{-8}\,\text{m}^3\,\text{s}^{-1}$. (*c*) Composite image of several camera images showing the upper 51 mm of the jet. (*a*) ×, experiment; —, theory; - - -, acceleration. (*b*) - - -, strain rate; . . . , velocity.

5.3. *Stationary experiments*

Figure 8 shows a typical stationary jet contour near the line of marginal stability. This stationary experiment demonstrates the capabilities of our optical measurement system and shows the different flow regimes. Experimental jet radii and numerical computations using (2.13) and (2.14) are in excellent agreement. Jet acceleration, strain rate and velocity are obtained using the same equations. Similar experiments were carried out for AK1000 ($d^* = 2.10\,\text{mm}$, $\dot{V} = 6.93 \times 10^{-8}\,\text{m}^3\,\text{s}^{-1}$), AK5000 ($d^* = 2.10\,\text{mm}$, $\dot{V} = 5.64 \times 10^{-8}\,\text{m}^3\,\text{s}^{-1}$) and AK50000 ($d^* = 3.12\,\text{mm}$, $\dot{V} = 6.04 \times 10^{-8}\,\text{m}^3\,\text{s}^{-1}$) with similarly good agreement to the theory. Using our non-dimensionalization, all these stationary solutions differ only slightly. For values of the non-dimensional volume flux $q \gg 1$, q has very little influence on the jet shape. This is the case here.

For a creeping Newtonian jet, Dutta & Ryan (1982) found, that 'the exit region, within which flow rearrangement occurs from Poiseuille to uniform plug flow, extends approximately from $z = -1$ to $z = 1.5$', where $z = 2x^*/d^*$. Therefore, theory and experiment show slight deviations in the direct neighbourhood of the nozzle.

It is not our aim to perform a comprehensive experimental study on the stationary jet shape. This is done elsewhere. Adachi *et al.* (1990) try to find a simple approximative function describing the jet shape over a wide range of outflow conditions fitting their experimental data. They do not compare to a numerical integration of the stationary equations.

The jet in figure 8 exits the nozzle at low velocity, low acceleration and moderate strain rate. The strain rate rises almost linearly with x^*, denoting the viscosity dominated region. The jet velocity rises quadratically with x^*. After a maximum strain

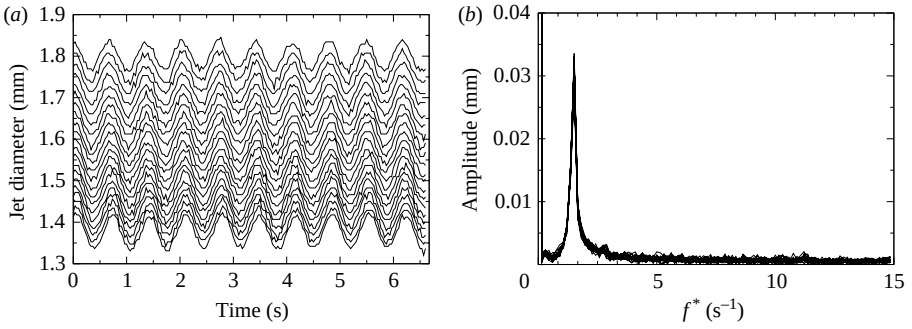

FIGURE 9. (*a*) Oscillation of a jet. The separate curves represent different vertical positions. AK5000, $d^* = 2.55$ mm, $\dot{V}^* = 6.75 \times 10^{-8}$ m^3 s^{-1}. (*b*) Corresponding Fourier transform.

rate at the transition from viscosity dominated to inertia dominated flow, the strain rate falls, tending to zero far downstream as velocity approaches $u^*_\infty = \sqrt{2gx^*}$. Jet acceleration rises monotonically approaching the free-fall limit of $g = 9.81$ m s^{-2}.

Figure 8(*c*) is a composite camera image showing the upper 51 mm of the jet. This illustrates what we think of when speaking of a slender jet and should not be confused with the strongly compressed diagram to the left. A light strip in the centre of the images results from the transmitted light of the back lighting.

5.4. *Experimental stability analysis*

Jet stability is studied as follows. Beginning with a stable stationary jet, flow rate is lowered slowly, until the whole jet up to the nozzle begins to oscillate. At any vertical position of the jet, the jet diameter oscillates periodically. This state is considered as unstable. Then the flow rate is increased again until the oscillation terminates, then lowered again and so forth. Following this procedure, the 'point' of marginal stability can be found within one step of the converter that controls the motor of the gear pump. In particular, the test fluids of highest viscosity showed very low growth rates and decay rates of perturbations in the proximity of the 'point' of marginal stability. Therefore one has to wait for a very long time (about half an hour for the test fluids of highest viscosity) until oscillations have ceased when coming from the unstable side and exceeding the 'point' of marginal stability by one converter step that is about 1 % to 2 % of the total volume flux. Coming from the stable side, the same picture is found. Within the range of one frequency converter step no hysteresis phenomenon could be found. One frequency converter step below the 'point' of marginal stability, the frequency of the oscillation is determined. A series of pictures is taken with the CCD camera. For each picture the jet diameter is identified at several vertical positions. An example of the result of this approach can be seen in figure 9 together with the corresponding discrete Fourier transform. The most unstable angular frequency, the so-called critical frequency ω^*_{crit}, can be calculated from the peak of this diagram by $\omega^*_{crit} = 2\pi f^*$. The distance between the vertical positions corresponding to the upper and the lower curve in figure 9(*a*) is 3.5 mm, the average local wave velocity is about 48 mm s^{-1}. Therefore the dilatations and contractions seem to occur almost at the same time at all vertical positions of this image section.

The measured points of marginal stability and the corresponding critical frequencies are given in figures 10 and 11. Theoretical predictions and experimental results are in good agreement. The strong deviations in marginal stability for the points of lowest nozzle exit velocity u_0 for AK1000, AK5000 and AK10000 are due to a violation

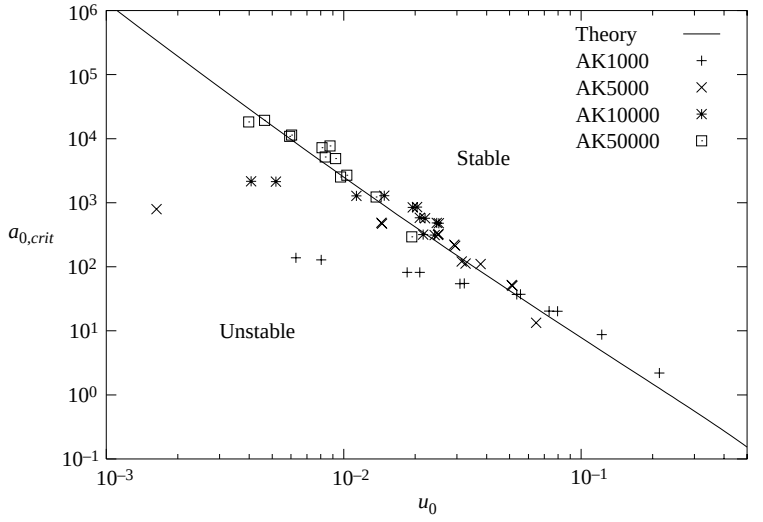

FIGURE 10. Theoretically predicted line of marginal stability and experimentally obtained points of marginal stability.

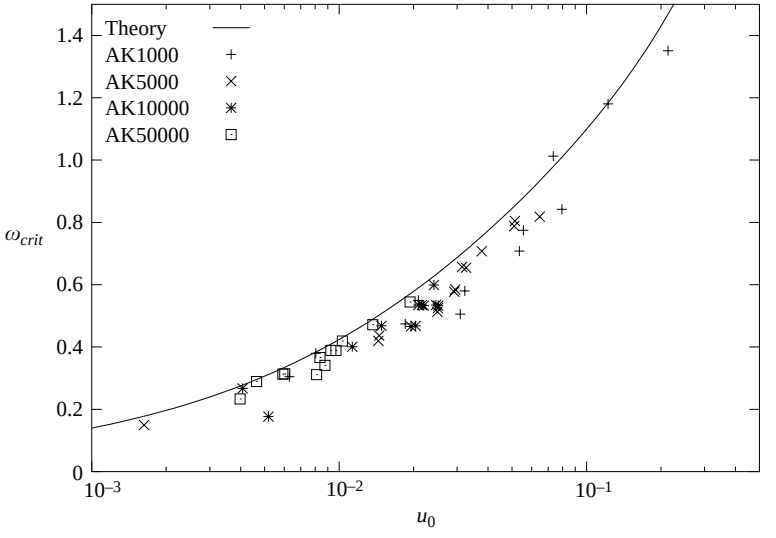

FIGURE 11. Theoretically predicted critical frequencies with experimental results.

of the slenderness assumption near the nozzle. This leads to enhanced stability that cannot be explained by the leading-order one-dimensional approximation used in the theoretical study.

5.5. *Slenderness criterion*

By introducing a new dimensionless parameter and further exploiting the one-dimensional theory, we can find a qualitative criterion for slenderness in the sense of our theory, which can be made a quantitative criterion using our experimental results. Obviously, the variation of the jet diameter d^* with axial position x^* is a good measure for slenderness at the orifice (we keep in mind that on the first one or two diameters distance from the orifice, the assumption of purely extensional flow does not hold, but

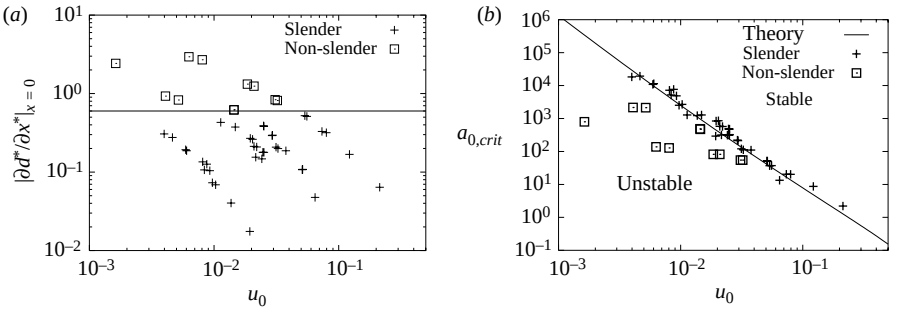

FIGURE 12. (*a*) $|\partial d^*/\partial x^*|_0$ as a slenderness criterion. Experimental points above the line $|\partial d^*/\partial x^*|_0 = 0.6$ show strong deviations from the theoretical line of marginal stability in (*b*).

that should not worry us too much). Incorporating our non-dimensionalization into

$$d^* = \sqrt{\frac{4}{\pi} a^*}, \tag{5.1}$$

we obtain

$$d^* = 2\sqrt{a}\left(\frac{\gamma^3}{\eta_D^2 g^2 \rho}\right)^{1/3}. \tag{5.2}$$

Differentiation with respect to x^* gives us a new dimensionless variable

$$\frac{\partial d^*}{\partial x^*} := 2\frac{\partial \sqrt{a}}{\partial x}\left(\frac{\gamma^3 \rho}{\eta_D^4 g}\right)^{1/3}. \tag{5.3}$$

In the viscosity dominated flow regime,

$$u = \tfrac{1}{2}(x + \sqrt{2u_0})^2 \tag{5.4}$$

gives a good approximation for the axial velocity if $u < 0.2$ and $q \gg 1$. Evaluating (5.3) at $x = 0$ using this approximation gives us

$$\left|\frac{\partial d^*}{\partial x^*}\right|_0 = \sqrt{\frac{2a_0}{u_0}}\left(\frac{\gamma^3 \rho}{\eta_D^4 g}\right)^{1/3}. \tag{5.5}$$

In figure 12(*a*), $|\partial d^*/\partial x^*|_0$ is plotted against u_0. Comparison with figure 12(*b*) gives us an approximate criterion for slenderness in the sense of our stability theory,

$$\left|\frac{\partial d^*}{\partial x^*}\right|_0 < 0.6. \tag{5.6}$$

The failure of the slenderness assumption can be seen in the shape of the filament. The value of $|\partial d^*/\partial x^*|_0 = 0.6$ gives a critical angle to the vertical axis of $\approx 17°$. The experimentally observed angles that can be extracted from digital images of the jet at the nozzle exit are smaller than the theoretically predicted angles. Quantitative agreement is not expected since flow rearrangement from shear flow to extensional flow takes place at the nozzle exit ($x = 0$).

6. Comparison to related problems

As mentioned in § 1, Le Dizès (1997) carried out a global linear stability analysis in falling capillary jets in the limit of high Reynolds numbers. His critical

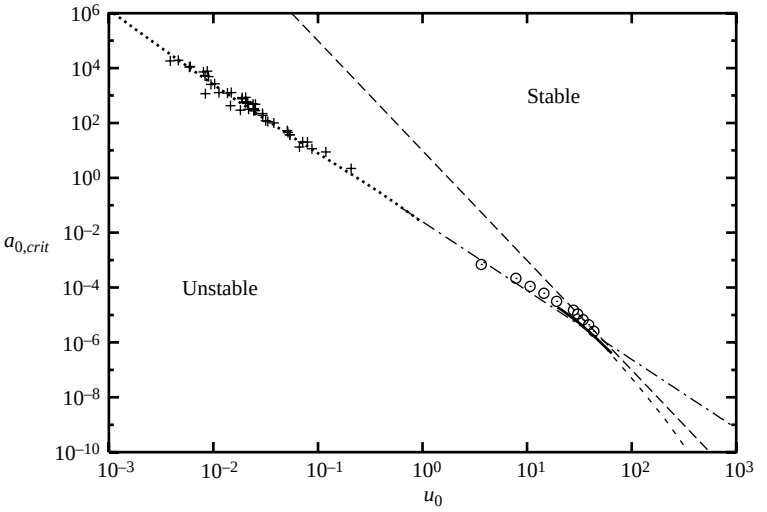

FIGURE 13. Our theory (···) and experiments (+) omitting the points violating our slenderness criterion. Extrapolation of our theory (– · –). Le Dizès (1997): global transition for a jet of water at high Reynolds numbers (———). Leib & Goldstein (1986*a*): transition to local absolute instability at the orifice for a non-viscous capillary jet (– – –). Leib & Goldstein (1986*b*): absolute instability of a viscous liquid jet of water without gravity (- - -). Clanet & Lasheras (2003): transition from dripping to jetting for a vertical falling jet of water (○).

parameters can be expressed in terms of our critical parameters: $u_0 = (Re/(3\,\varepsilon))^{1/3}$ and $a_{0,crit} = We^{-2}(Re/(3\,\varepsilon))^{-4/3}$, where the Reynolds and Weber numbers are defined as in § 1 and the slenderness parameter $\varepsilon = Fr^{-2}$ is connected to the Froude number. Le Dizès performed an example calculation for high Reynolds numbers using the physical parameters of water. The curve shown in figure 13 is read off his diagrams and represents the validity range of his theory. A straight line with a slope of -4 in the log–log diagram represents the value $We = 0.32$ for the transition to local absolute instability at the orifice in the non-viscous limit found by Leib & Goldstein (1986*a*). Leib & Goldstein (1986*b*) give the transition to absolute instability for a viscous liquid jet without gravity. Our dimensionless parameters expressed in terms of their critical Rayleigh and Weber numbers read: $u_0 = 6\,We/Re(\rho\gamma^3/\eta_D^4 g)^{1/3}$ and $a_{0,crit} = Re^4/We^2(\rho\gamma^3/\eta_D^4 g)^{-4/3}/1296$. The curve given in figure 13 is read from their stability diagram and represents the range of their calculated values. In figure 13, we can see the difference between the high Reynolds number and inviscid global stability results obtained from local considerations and our global stability analysis for a very viscous fluid jet under gravity.

Clanet & Lasheras (1999) study the transition from dripping to jetting for an inertia dominated flow. The dimensionless parameters and the validity range of their theory are given in § 1. They carry out experiments using hypodermic needles as nozzles with a thick-walled completely wetted nozzle exit and deionized water as test fluid. Because of the finite wall thickness at the nozzle exit, it is difficult to introduce their experimental findings into our diagram, but we still want to do so. From the given Reynolds ($Re = V_0\,D/\nu$, with V_0 as the area averaged outflow velocity and D as the inner diameter of the nozzle) and Weber numbers, we calculate our parameters through $u_0 = 3\,We/Re\,(\rho\gamma^3/(\eta_D^4 g))^{1/3}$ and $a_{0,crit} = Re^4/(We^2(18\,(\rho\gamma^3/(\eta_D^4 g))^{2/3})^2)$. We somewhat arbitrarily choose the inner diameter to build the Bond number (Weber

and Reynolds numbers always use the inner diameter). The result of this procedure can be seen in figure 13. It is remarkable, that the experimental values of Clanet & Lasheras are very close to an extrapolation of our theory, although being taken in a completely different parameter range and describing the transition from dripping to jetting rather than the instability of a long jet.

7. Conclusion

Linear stability analysis was applied to the leading-order one-dimensional theory of a vertical liquid Newtonian jet with inertia and surface tension present torn down by gravity and exhibiting a sufficiently long viscosity-dominated zone near the orifice. A line of marginal stability as well as the corresponding most unstable frequencies are obtained. These describe a global instability that occurs when, for a given dimensionless nozzle cross-section, the dimensionless outflow velocity falls below a limit given by the line of marginal stability.

An experimental study was carried out to support the theoretical findings. Theoretical and experimental results are in excellent agreement. The line of marginal stability as well as the most unstable frequencies could be confirmed with a standard deviation of less than 15 % omitting the experimental values violating our semi-empirical slenderness criterion (equation (5.6)). An approximative function (equation (3.31)) for the line of marginal stability is given.

Nonlinear simulations are carried out in the neighbourhood of the line of marginal stability, showing limit cycles in the unstable regime and a strongly decreasing disturbance amplitude in the stable regime. Performing random sampling with nonlinear simulations, no subcritical bifurcating solutions (being unstable in the linearly stable regime) could be found.

This work was supported by the Deutsche Forschungsgemeinschaft (DFG). Thanks are due to Professor P. Rentrop for providing a solver for the multiple shooting Runge–Kutta–Fehlberg method.

REFERENCES

Adachi, K., Tagashira, K., Banba, Y., Tatsumi, H., Machida, H. & Yoshioka, N. 1990 Steady laminar round jets of a viscous liquid falling vertically in the atmosphere. *AIChE J.* **36**, 738–745.

Bechtel, S. E., Forest, M. G. & Bogy, D. B. 1986 A one-dimensional theory for viscoelastic fluid jets, with application to extrudate-swell and draw-down under gravity. *J. Non-Newt onian Fluid Mech.* **21**, 273–308.

Bechtel, S. E., Lin, K. J. & Forest, M. G. 1987 Effective stress rates of viscoelastic free jets. *J. Non-Newt onian Fluid Mech.* **26**, 1–41.

Boyer, R. F. & Spencer, R. S. 1944 Thermal expansion and second-order transition effects in high polymers. *J. Appl. Phys.* **15**, 398–405.

Chandrasekhar, S. 1961 *Hydrodynamic and Hydromagnetic Stability*. Oxford University Press. (Reprinted 1981, Dover, New York).

Clanet, C. & Lasheras, J. C. 1999 Transition from dripping to jetting. *J. Fluid Mech.* **383**, 307–326.

Clarke, N. S. 1966 A differential equation in fluid mechanics. *Mathematika* **12**, 51–53.

Clarke, N. S. 1969 The asymptotic effects of surface tension and viscosity on an axially-symmetric free jet of liquid under gravity. *Q. J. Mech. Appl. Maths* **22**, 247–256.

Dutta, A. & Ryan, M. E. 1982 Dynamics of a creeping Newtonian jet with gravity and surface tension: a finite difference technique for solving steady free-surface flows using orthogonal curvilinear coordinates. *AIChE J.* **28**, 220–232.

Eggers, J. 1997 Nonlinear dynamics and breakup of free-surface flows. *Rev. Mod. Phys.* **69**, 865–929.

Grant, R. P. & Middleman, S. 1966 Newtonian jet instability. *AIChE J.* **12**, 669–678.

Guggenheim, E. A. 1945 The principle of corresponding states. *J. Chem. Phys.* **13**, 253–261.

Haenlein, A. 1931 Über den Zerfall eines Flüssigkeitsstrahles. *Forsch. Ing. Wes.* **2**, 139–149.

Joseph, D. D., Nguyen, K. & Matta, J. E. 1983 Jets into liquid under gravity. *J. Fluid Mech.* **128**, 443–468.

Kase, S. & Matsuo, T. 1967 Studies on melt spinning: II. Steady-state and transient solutions of fundamental equations compared with experimental results. *J. Polymer Sci.* **11**, 251–287.

Kase, S., Matsuo, T. & Yoshimoto, Y. 1966 Theoretical analysis of melt spinning. Part 2. Surging phenomena in extrusion casting of plastic films. *Seni Kikai Gakkai Shi (Japanese Journal of Textile Machinery)* **19**, 62–72.

Kaye, A. & Vale, D. G. 1969 The shape of a vertically falling stream of a Newtonian liquid. *Rheol. Acta* **8**, 1–5.

Kitamura, Y., Shigeta, H., Kawata, T. & Takahashi, T. 1987 Breakup of non-Newtonian emulsion jets. *Can. J. Chem. Engng* **65**, 202–209.

van Krevelen, D. W. 1990 *Properties of Polymers.* Elsevier.

Larson, R. G. 1992 Review: instabilities in viscoelastic flows. *Rheol. Acta* **31**, 213–263.

Le Dizès, S. 1997 Global modes in falling capillary jets. *Eur. J. Mech.* B/*Fluids* **16**, 761–778.

Leib, S. J. & Goldstein, M. E. 1986*a* The generation of capillary instabilities on a liquid jet. *J. Fluid Mech.* **168**, 479–500.

Leib, S. J. & Goldstein, M. E. 1986*b* Convective and absolute instability of a viscous liquid jet. *Phys. Fluids* **29**, 952–954.

Mahadevan, L., Ryu, W. S. & Samuel A. D. T. 1998 Fluid 'rope trick' investigated. *Rheol. Acta* **31**, 213–263.

Monkewitz, P. A. 1990 The role of absolute and convective instability in predicting the behaviour of fluid systems. *Eur. J. Mech.* B/*Fluids* **9**, 395–413.

Nonnenmacher, S. 2003 Numerische und experimentelle Untersuchungen zur Restentgasung in statischen Entgasungsapparaten. PhD thesis, Universität Stuttgart.

Pearson, J. R. A. & Matovich, M. A. 1969 Spinning a molten threadline: stability. *Ind. Engng Chem. Fund.* **8**, 605–609.

Pearson, J. R. A. & Shah, Y. T. 1972 Stability analysis of the fiber spinning process. *Trans. Soc. Rheol.* **16**, 519–533.

Petrie, C. J. S. & Denn, M. M. 1976 Instabilities in polymer processing. *AIChE J.* **22**, 209–236.

Plateau, J. 1849 Recherches expérimentales et théoriques sur les figures d'équilibre d'une masse liquide sans pesanteur. *Acad. Sci. Bruxelles Mém* **23**, 1–155.

Rayleigh, Lord J. W. S. 1878 On the stability of jets. *Proc. Lond. Math. Soc.* **10**, 4–13.

Rayleigh, Lord J. W. S. 1892 On the stability of a cylinder of viscous fluid under a capillary force. *Phil. Mag.* **34**, 145–154.

Savart, F. 1833 Mémoire sur la constitution des veines liquides lancées par des orifices circulaires en mince paroi. *Ann. Chim. Phys.* **53**, 337–386.

Stoer, J. & Bulirsch, R. 1978 *Einführung in die Numerische Mathematik II.* Springer.

Tate, T. 1864 On the magnitude of a drop of liquid formed under different circumstances. *Phil. Mag.* **27**, 176–180.

Tchavdarov, B., Yarin, A. L. & Radev, S. 1993 Buckling of thin liquid jets. *J. Fluid Mech.* **253**, 593–615.

Weber, C. 1931 Zum Zerfall eines Flüssigkeitsstrahles. *Z. angew. Math. Mech.* **11**, 136–154.

Wilson, S. D. R. 1988 The slow dripping of a viscous fluid. *J. Fluid Mech.* **190**, 561–570.

Wu, S. 1982 *Polymer Interface and Adhesion.* Dekker.